

Article

Simulations and Tests of a KRET Aerospace Penetrator

Krzysztof Bieńkowski ¹, Łukasz Kolimas ² , Sebastian Łapczyński ², Michał Drogosz ³,
Michał Szulborski ^{2,*} , Łukasz Wiśniewski ¹, Bartosz Kędziora ¹ and Łukasz Kozarek ² 

¹ Astronika Sp. z o.o., ul. Bartycka 18, 00-716 Warsaw, Poland; krzysztof.bienkowski@gmail.com (K.B.); lwisniewski@astronika.pl (Ł.W.); bkedziora@astronika.pl (B.K.)

² Institute of Electrical Power Engineering, Warsaw University of Technology, 00-662 Warsaw, Poland; lukasz.kolimas@ien.pw.edu.pl (Ł.K.); seb.lapczynski@gmail.com (S.Ł.); lukaszkozarek@gmail.com (Ł.K.)

³ Syderal Sp. z o.o., ul. Trzy Lipy 3, 80-172 Gdansk, Poland; michal.drogosz@syderal.pl

* Correspondence: michal.szulborski.dokt@pw.edu.pl; Tel.: +48-662-119-014

Received: 17 March 2020; Accepted: 24 June 2020; Published: 26 June 2020



Abstract: This manuscript presents the simulation tests of an aerospace penetrator conducted to check the device's validity and functionality. For this work, the numerical model was created on the basis of engineering data, the laboratory model of the tube reluctance actuator was created on the basis of the numerical model, and a set of simulations were executed on the basis of both presented. Moreover, the mathematical model was supplemented by precise boundary conditions. The main goal was the analysis of the introduced device's properties by comparing them to experimental values. Three different variants were taken into account to check the construction functionality and to study the most important parameters, e.g., the hammer displacement, hammer velocity, eddy currents and overall electromagnetic properties of the penetrator's hammer displacement. The high-end values of the applied components were derived on the basis of the results and are presented in the summary of the concluded work. An overall method for checking the validity of the penetrator was proposed, which is cost and time effective. The model used was not limited in the representation of physical phenomena.

Keywords: reluctance actuator; aerospace penetrator; FEM; simulation; mole penetrator; KRET; analysis

1. Introduction

Soil penetrators are research instruments used in space missions for scientific and technical purposes. The examined space entities can be either small bodies—asteroids, comets, and larger objects; planets; or moons. Penetrators are used to conduct scientific research and carry out the following technical tasks:

- Soil mechanics analysis;
- Chemical and mineralogical analysis;
- Thermal tests (e.g., measurement of the temperature under the body surface, thermal conductivity);
- Electrical and magnetic research;
- Soil sampling for further analysis or delivery on a return mission to Earth;
- Transporting and placing other components in a given soil;
- Anchoring objects.

In general, penetrators can be divided into impactors (kinetic penetrators), which are characterized by having a very high initial speed while breaking under the surface. The second types are stationary penetrators, which are used after landing on a given body.

Impactors are used in missions where landing is not provided. Their advantages include the high kinetic energy of the impact and thus great opportunities to sink under the surface. The disadvantage of this type of solution is the huge overloads that can damage sensors or other research components. An example of a mission in which the impactor was used is the NASA Deep Impact mission [1]. Stationary penetrators are characterized by a relatively low driving speed. Two methods of insertion are distinguished—drilling and driving. The first method is used to sink or take samples from hard materials. This device of this type was used on the European Space Agency (ESA) rover during the ExoMars 2018 mission [1]. Drilling seems to be the most obvious way to break below the surface. However, in the case of space missions, it has several major disadvantages, such as high forces affecting the lander/platform or relatively high energy consumption.

In the case of hammering, two methods of soil penetration can be distinguished: penetration during one short continuous process or discreet penetration by repeating the hammer action. An example of a continuous hammering penetrator is the PHILAE harpoon of the Rosetta mission [2–5] presented in Figure 1. The drive used in this case was a compressed gas cartridge. These harpoons were used to anchor the lander immediately after contact with the comet and enable it to further carry out its mission. However, the devices did not work properly, which was one of the main reasons for Rosetta's mission goals not being fully realized. Generally, a big problem with this type of penetrator (moving in fast motion) is the cable unrolling (especially at low temperatures) and the inability to control the thrust and one-off operation.



Figure 1. PHILAE lander harpoon used in the Rosetta mission [2].

The last of the currently used devices in space missions to penetrate the surface of celestial bodies are penetrators characterized by low-velocity penetration. The main executive element in this type of solution is the so-called hammer. The component is accelerated and then hits the housing, resulting in the breaking of the surface (usually a few millimeters). A very important feature of this type of construction is the energy accumulator, which is—depending on the design—a capacitor (electrical energy) or a spring (mechanical energy). One of the institutions in the world where low-speed penetrator technologies are being developed is the Space Research Center (CBK) of the Polish Academy of Sciences. Examples of penetrators with a battery in the form of a capacitor are MUPUS [6] and CHOMIK [7]—a penetrator developed for the Phobos Grunt mission. The driving unit of both penetrators is an electromagnet with a movable dive (hammer), shown in Figure 2.

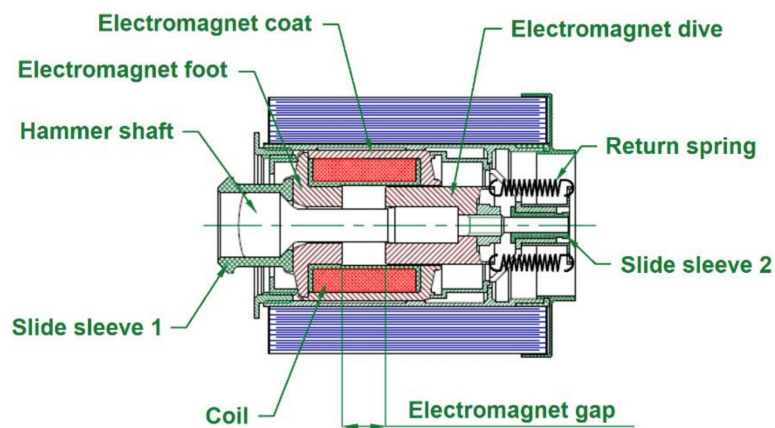


Figure 2. MUPUS and CHOMIK penetrator drive unit [6,7].

The pulling of the dive inside is caused by the creation of a ponderomotive force seeking to reduce the gap. The return of the dive (hammer) to the starting position is ensured by two small return springs with low pressure. A hammer hitting the foot causes the test rod (MUPUS) or soil sample container (CHOMIK) to sink. The penetrators are shown in Figure 3.

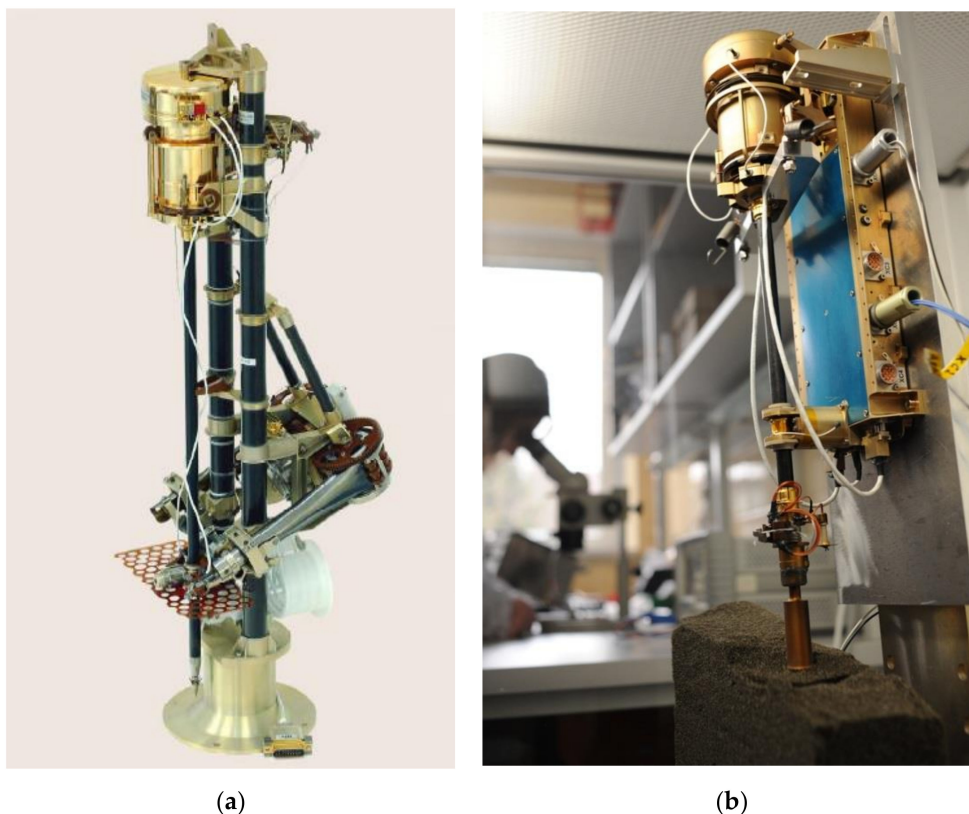


Figure 3. MUPUS (a) and CHOMIK (b) penetrators [6,7].

For both penetrators described above, the maximum driving depth is limited by the drive section. It means that those penetrators can sink to a maximum of about 30–40 cm, i.e., as much as the length of the test rod will allow. Mole-type penetrators do not have such a restriction. These devices are characterized by a compact construction with a small diameter, enabling the sinking of the entire penetrator into the hammered object. The only limiters of the penetration for this type of construction are the mechanical properties of the soil and the length of the power cable. The energy accumulator in this case is a spring compressed by an electric actuator. When the shortening is achieved, the

spring-retaining clip is released, which releases the energy that drives the hammer. The penetration of the penetrator is induced by the hitting of the hammer against the casing tip. An example of this type of penetrator is KRET, shown in Figure 4.

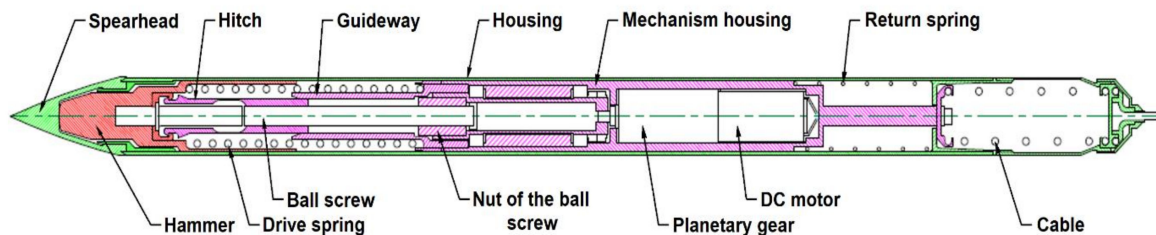


Figure 4. Cross-sectional view of the KRET penetrator developed by the Astronika Sp. z o.o. and the Warsaw University of Technology Team.

The KRET penetrator belongs to the group of self-piercing space penetrators. The task of the device is to provide small detectors (such as thermal sensors) under the surface of the body for scientific research. The depth of the penetration of the soil for Mars or the Moon is estimated at about 7 m. The instrument was developed to be placed on board lunar landers as part of the International Lunar Network initiative. Work is currently underway to integrate KRET with the Lunar Geophysical Investigation Package as part of the NASA project. Thanks to measurements carried out with the help of this device, it will be possible to determine, among other things, the value of the heat flux that reaches the surface of the Moon from its interior.

The KRET penetrator tube reluctance actuator construction and basic components are shown in Figures 5 and 6.

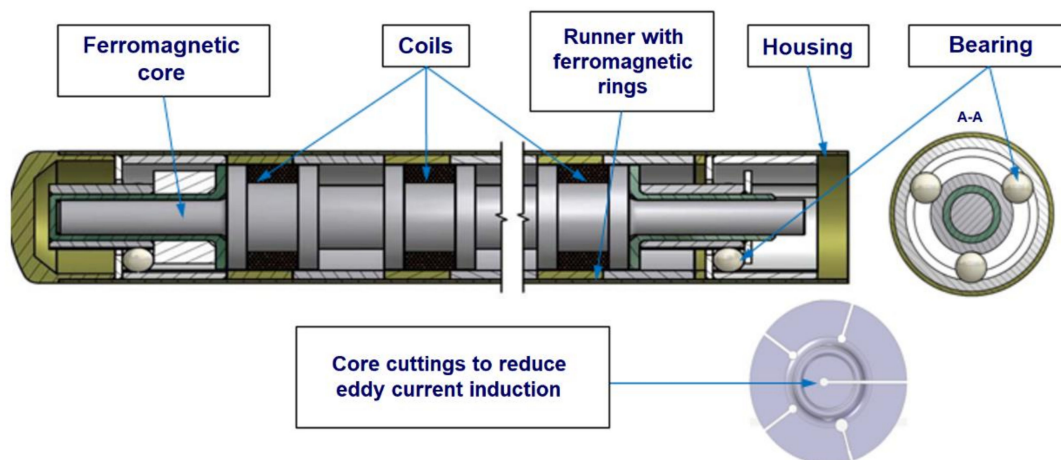


Figure 5. Construction of the penetrator drive system (tube reluctance actuator) used in the KRET penetrator.

Environmental conditions are very important factors affecting the construction of all penetrators. Some examples of the requirements for this type of equipment are [8–14]:

- The ability to work in a very large temperature range (depending on the mission, the minimum temperature can reach $-160\text{ }^{\circ}\text{C}$);
- A low weight of the device;
- Restrictions on power access;
- A long flight time (up to 12 years depending on the mission);
- Resistance to overload at startup;
- The ability to operate in a vacuum.

The numerical model described in this chapter was developed from scratch using the APDL language. This requires a greater effort at the model creation stage; however, thanks to this approach, the process of making changes in the construction parameters is not a problem. The most arduous processes in creating FEM models (such as creating geometry and division into finite elements) have been properly implemented and parameterized while creating the basic model, which allows their automatic execution. The methods of executing the numerical methods are shown in Figure 7, and the individual steps to create a model are shown in Figure 8 below [24–27].

The numerical model directly takes into account the dynamic interactions between the three physical phenomena needed to simulate the operation of the device: electricity, magnetism, and dynamics. The figure shows, schematically, the components that have been included in the numerical model. Due to the construction of the device, the field submodel was simulated with a two-dimensional geometry, taking into account axial symmetry. The peripheral submodel is directly coupled to the field submodel by coupling the properties and degrees of freedom of the coils (Figure 9). As already mentioned, the model combines three different physical phenomena and finds a solution in the time domain (transient analysis) [28–30].

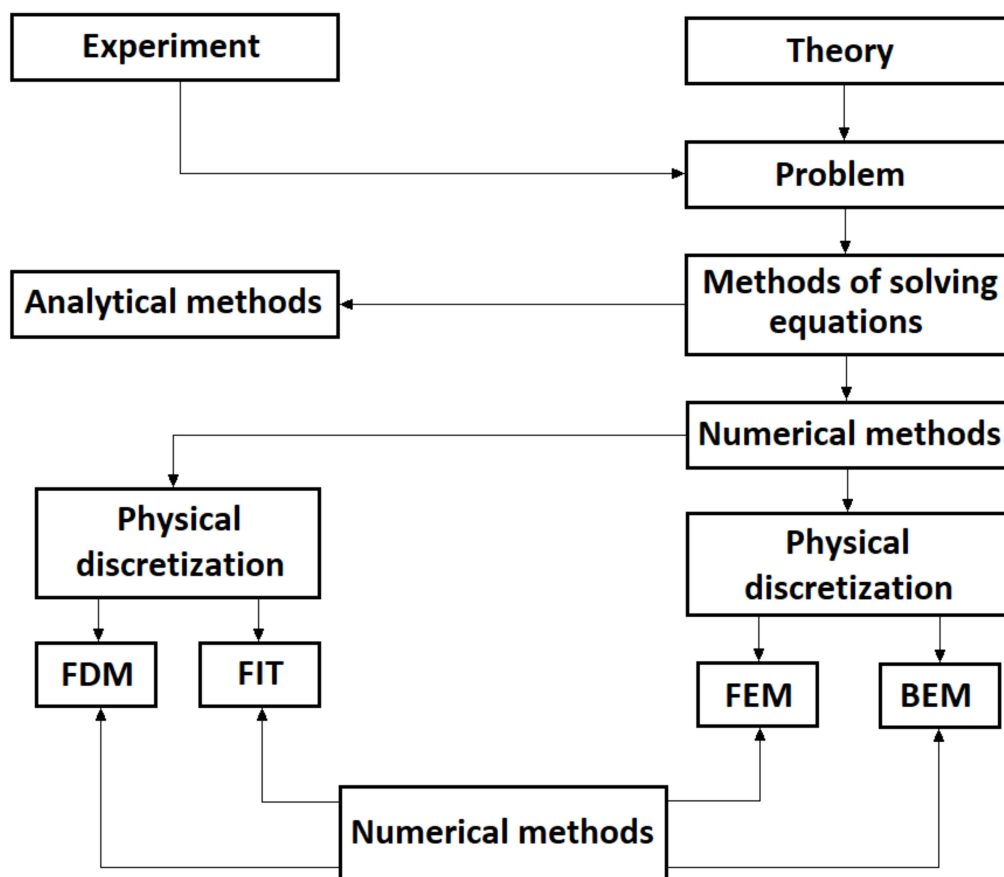


Figure 7. Schematic diagram showing the execution of numerical methods.

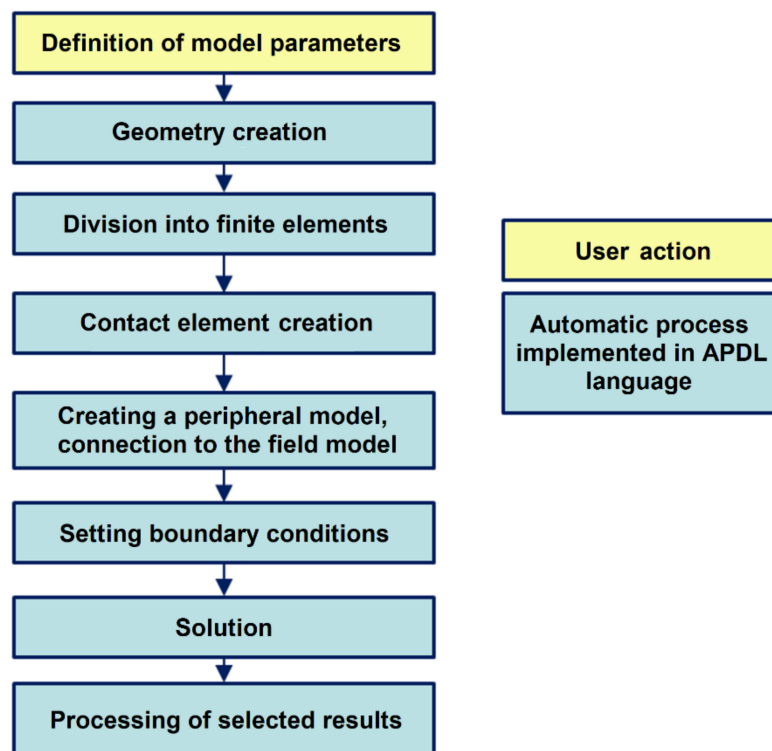


Figure 8. Individual stages of creating a numerical model.

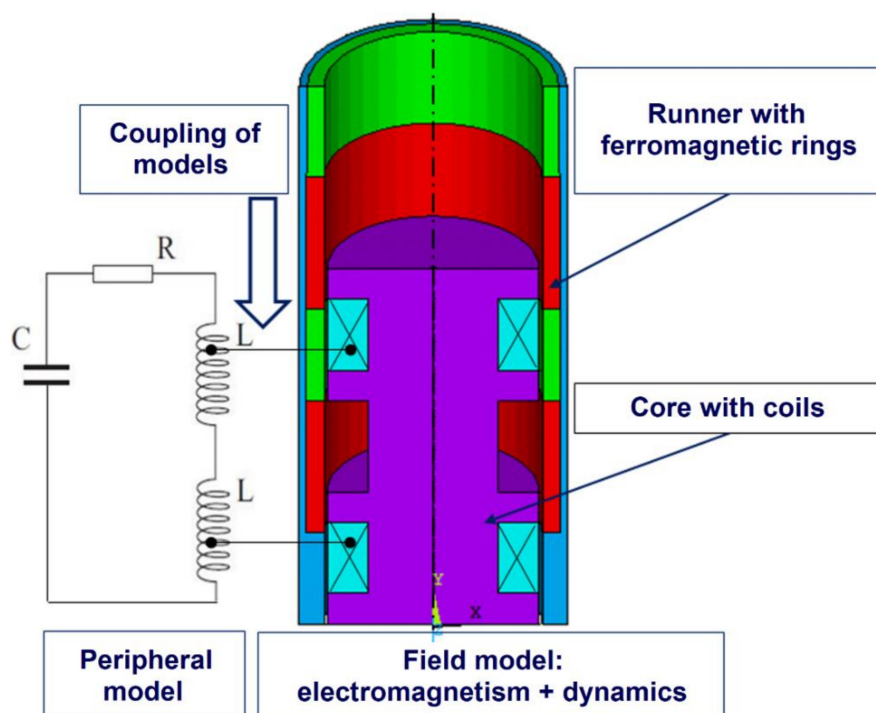


Figure 9. Components of the numerical model.

In order to simplify the model and reduce the number of finite elements, only two sections (coils) of the linear actuator are modeled (pre-estimated six sections on the entire device motors). Depending on the configuration of the construction parameters, after discretization, the model contains from 10 to 40 thousand finite elements. The model's mesh is compacted in critical areas (places of magnetic field density) in order to increase the accuracy of the obtained solution (Figure 10).

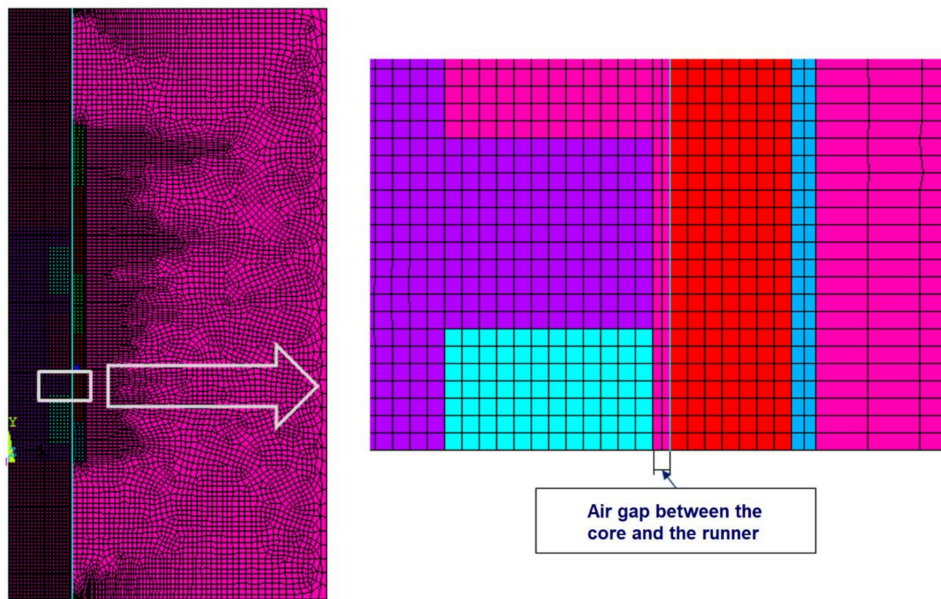


Figure 10. Field model divided into finite elements.

A single time step has been estimated at 0.00005 s, which provides a solution of about 80 steps to simulate a single device working action (depending on the configuration of the construction parameters). For each time step, the relative position between the core (counterweight) and the runner (hammer) is updated and included in the next time step. The displacement is carried out by moving elements simulating the runner along the contact elements. The model operation method is shown in Figure 11. In addition, the graphic presents a diagram showing the method of driving the device.

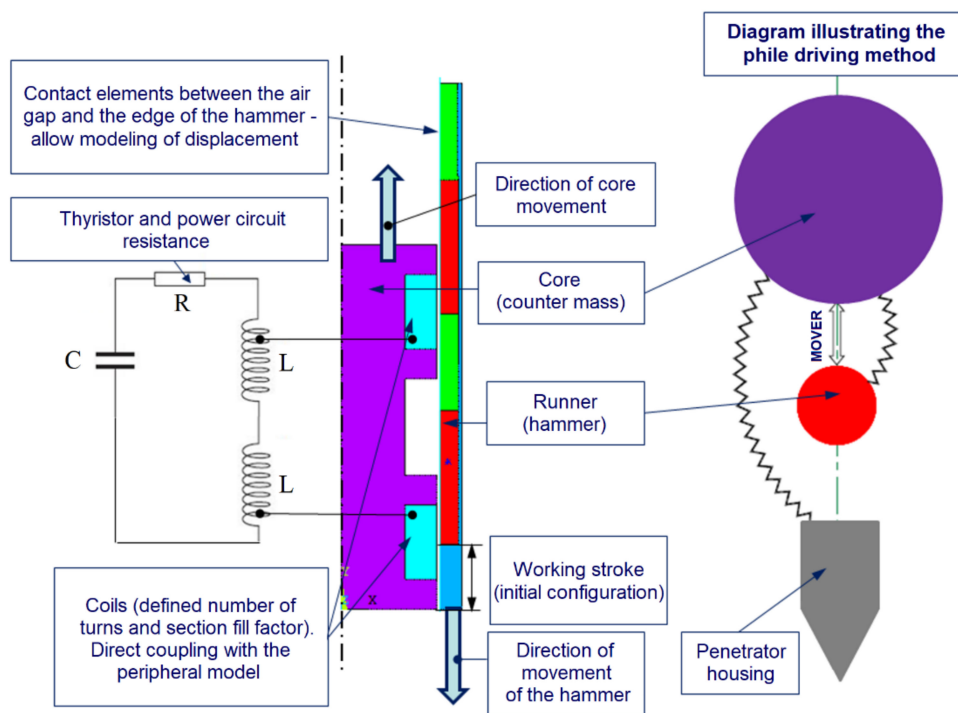


Figure 11. The principle of the numerical model operation.

3. Limitations of the Numerical Model

The numerical model used did not accurately reflect reality. Some phenomena were omitted due to their negligible impacts on the results of the calculations. The chosen modeling method also did not allow for the incorporation of some engine design features. The chapter explains the most important simplifications [31,32].

The first simplification concerned the aerodynamic drag. During the runner's working motion, aerodynamic drag occurred in the air. The value of the aerodynamic force depends mainly on the speed and drag coefficient, which is dimensionless, depending on the shape and orientation of the moving body. For the geometry of the runner, the resistance coefficient takes a relatively low value. Besides, the achieved speeds are also not low in terms of aerodynamic drag. Therefore, bypassing this phenomenon would not significantly affect the accuracy of the results [33–35].

The second simplification concerned the rolling friction. The developed model did not include rolling resistance in the linear bearing used in the mechanism construction. The rolling friction force is directly proportional to the clamping force. It should be noted that in the case of the mechanism under consideration, the engine generates a thrust that is perpendicular to the contact force of the bearing balls. The main role of linear bearings is to ensure axially between the core and the runner. Therefore, rolling frictional resistance has been omitted in the numerical analysis.

The third simplification concerned the geometry. Since the developed model is an axially symmetrical two-dimensional model, it presents an idealized system geometry (e.g., ideal engine axis). It also did not take into account an important design feature—undercuts in the motor core introduced to minimize the phenomenon of eddy current induction [36–38].

4. Laboratory Model of the Tube Reluctance Actuator

In order to check the validity of the penetrator concept and verify the calculations, a laboratory model of the actuator was developed and then produced. It should be noted that this model was designed on the basis of preliminary calculations. The laboratory model contains all the relevant components from the point of view of penetrator functionality and is built of the following elements:

- Hammer (runner);
- Anvil;
- Counter-weight;
- Counter-mass return spring;
- Linear ball raceway.

The construction of the device is shown in Figure 12 below.

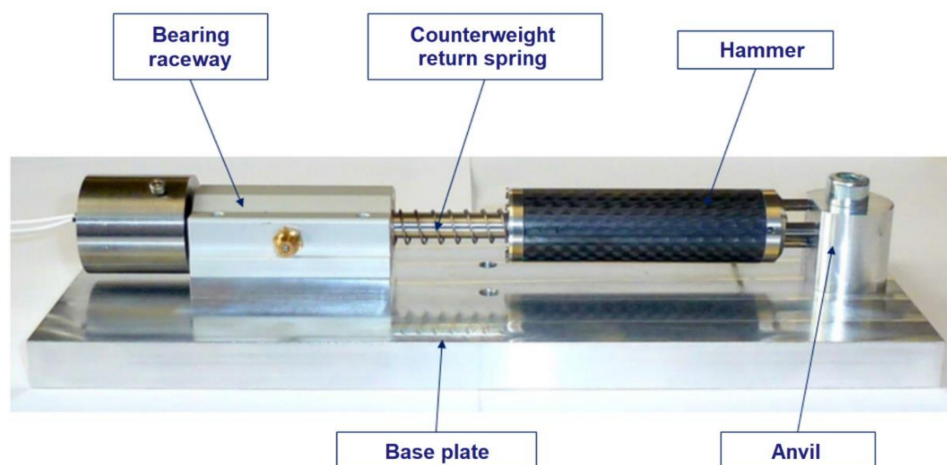


Figure 12. Laboratory model of the penetrator.

The main components of the hammer are ferromagnetic rings and a titanium tip—an element hitting the anvil. In addition, the hammer includes separators that are making a gap between two ferromagnetic rings and bearing raceways. All the components are connected by an external housing made of carbon fibers. Details regarding the construction of the hammer are shown in Figure 13.

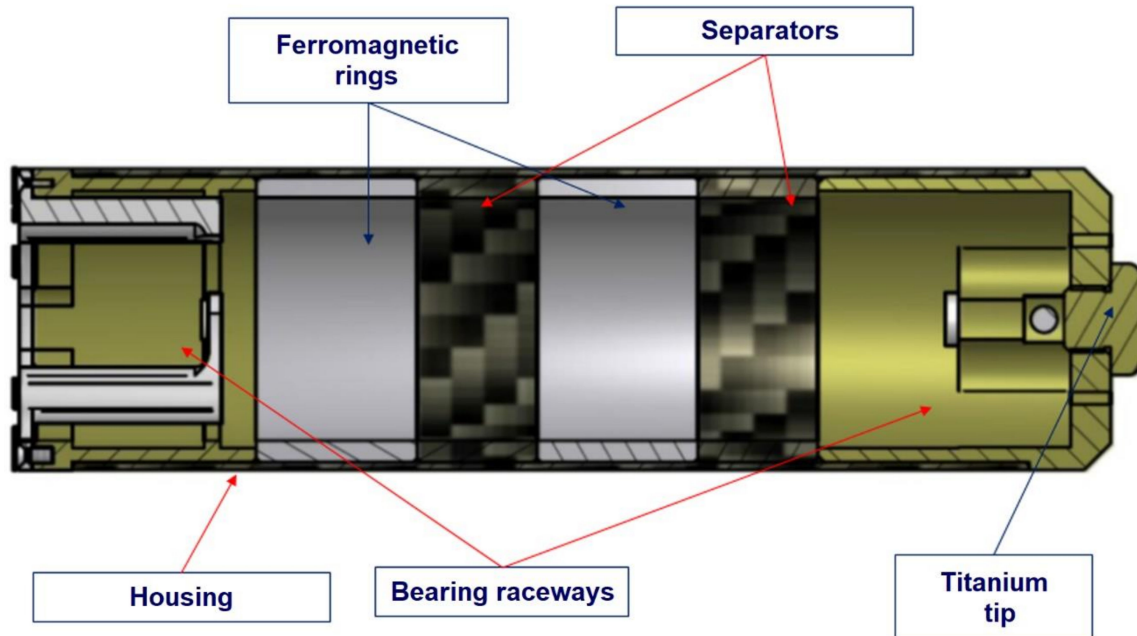


Figure 13. Cross-section showing hammer components.

The main counter-mass component is the core made of ferromagnetic material (the same as for hammer rings—ARMCO iron) with two coils wound. At both ends of the core, there are bearing raceways on which balls move, enabling the linear movement of the hammer. An element maintaining the initial distance between the hammer and the anvil—a stop—has been attached to one of the treadmills. On the opposite side, a guide rod is attached, which moves along the linear guide. An additional mass was placed at the end of the rod to ensure the correct mass ratio between the hammer and the counter-mass. The counter-mass module is shown in Figure 14 below.

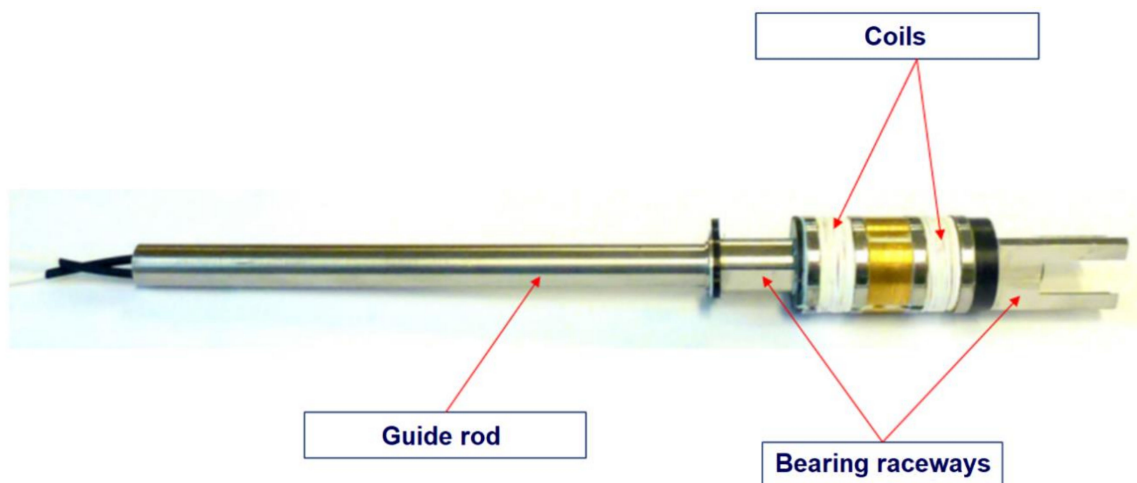


Figure 14. The counter-mass module.

Functional tests were performed in a vertical configuration (Figure 15). The control parameter examined during the functional tests was the displacement of the hammer vs. time (velocity). The measurements were made using a camera for fast video recording.



Figure 15. Test configuration of the laboratory model.

5. Laboratory Model Tests and Simulation Validity Check

The numerical model verification was based on the laboratory model. The parameter values recorded during the functional tests are the most important data concerning the penetrator's performance—the hammer velocity—and thus the kinetic energy impacting on the housing.

Figures 16–18 present a comparison of the results obtained by means of simulations and measurements performed during tests of the laboratory model. The reference parameter is the velocity of the actuator hammer (runner). The results are presented for three different values of the working stroke—parameter p .

It should be mentioned that the presented test results are averages of the measurements taken. In addition, the measurement results obtained are subjected to a rather significant error (estimated at even 10%). This is due to the method of data processing. The image recorded with the camera for the fast movement was analyzed “frame by frame”, determining the displacement of the hammer between the individual frames of the video. Based on the frequency at which the pictures were taken (0.12 ms), the speed characteristics were determined. The moment of the termination of the simulation and the tests carried out was assumed to be the moment of the alignment of the ferromagnetic rings.

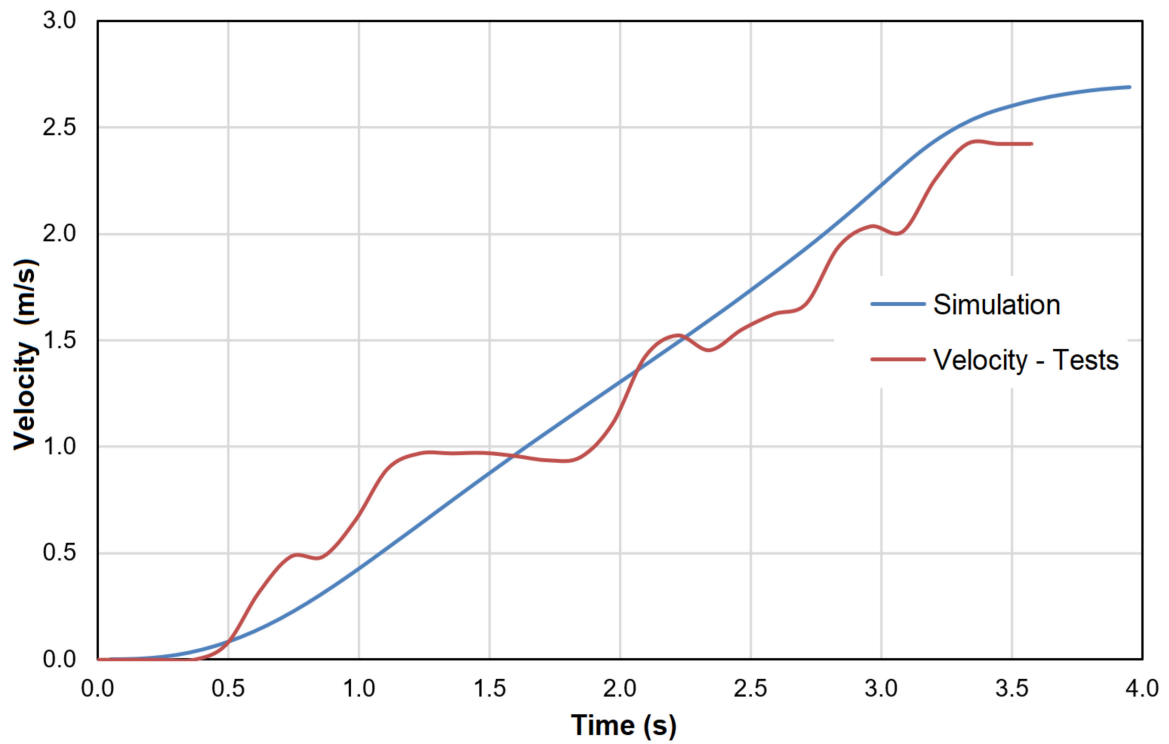


Figure 16. Comparison of velocity measurement results, and analysis of the results for the value of the working stroke $s = 6.5$ mm.

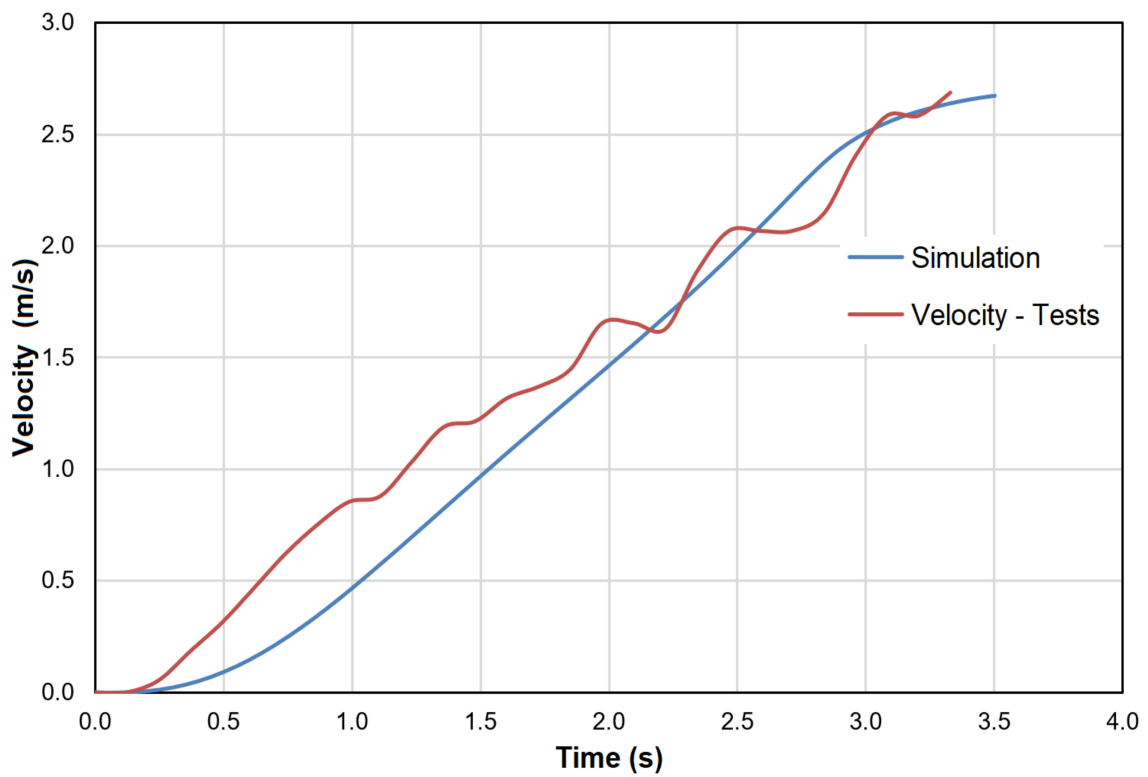


Figure 17. Comparison of velocity measurement results, and analysis of the results for the value of the working stroke $s = 6$ mm.

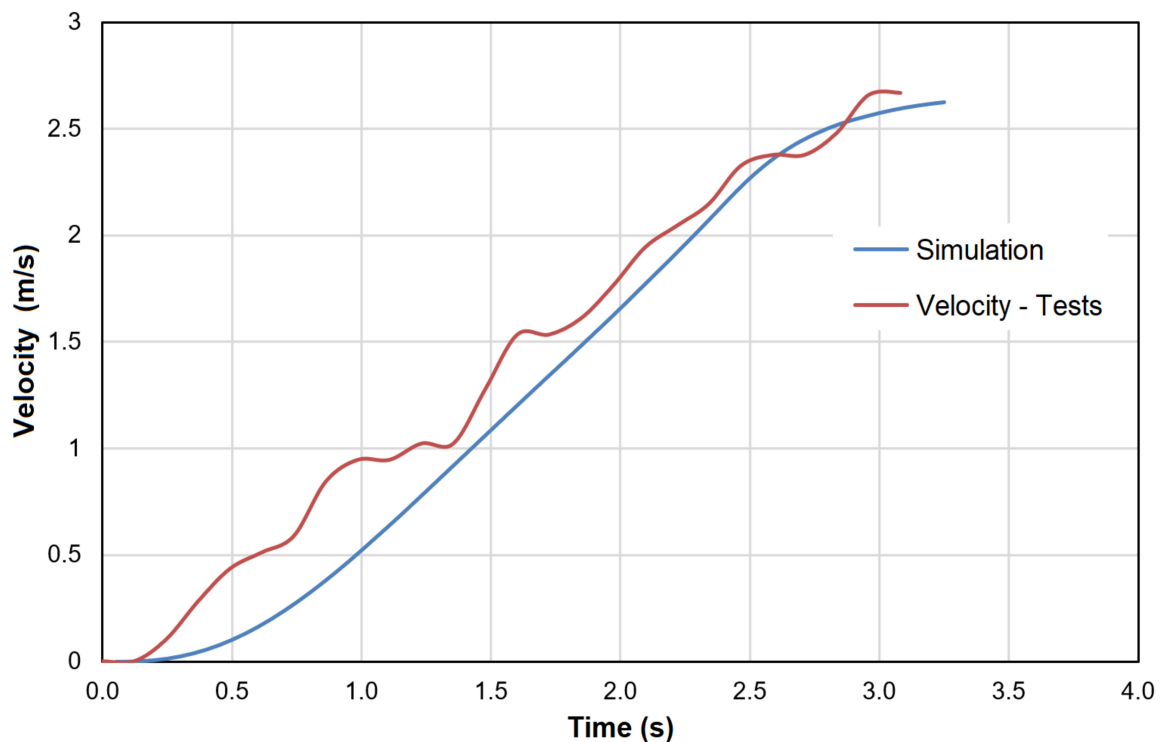


Figure 18. Comparison of velocity measurement results, and analysis of the results for the value of the working stroke $s = 5.5$ mm.

The developed laboratory model contains a basic construction error—the coil windings were wound in the same direction, which causes a significant reduction in the motor efficiency (adjacent poles are unlike). This error was detected after performing numerical analyses with correctly modeled coil windings. Nevertheless, for the verification of the numerical model, the simulation results are presented taking into account the incorrect return of the coil winding (and hence the return of the current flow).

The comparison of the hammer speed characteristics provided shows good compatibility of the simulation with the real object. Despite its complexity lying mainly in the direct coupling of the field and peripheral models, the direct modeling of the hammer displacement in the field model, and the taking into account of the phenomenon of eddy currents, the model consists of some simplifications. The most important simplification is the presentation of the actuator core model as having a plane geometry with axial symmetry. In fact, the core contains radial incisions to reduce the phenomenon of eddy current induction. Despite the omission of this design feature, the results of the tests and simulations carried out show very good compliance.

The authors are aware of a certain disadvantage of the model verification carried out in this way—the only checked parameters are the runner velocity of the model and electromagnetic phenomena that occur while the hammer is displaced. In order to verify the model more accurately, it would be necessary to carry out measurements of other physical quantities such as the discharge characteristics of the capacitor or current and voltage coil waveforms. However, at the project planning stage, it was decided to perform only the hammer velocity and displacement measurements, as those are the most important parameters for the device structure. The value of the velocity depends on the results of the electromagnetic analysis. The electrical energy accumulated in the capacitor is converted into magnetic field energy, which generates ponderomotive force and, finally, the displacement of the hammer. Given the above, it can be concluded that if the velocity results for the tests and simulations match, the entire energy conversion process occurs correctly. The results presented are therefore a sufficient basis for further simulations to determine the design parameters to ensure more efficient actuator operation.

6. Analysis of Simulation Results

This section presents the results of an actuator FEM simulation with design parameters for a laboratory model. The purpose of the result analysis is to find weak points in the structure and identify parameters that can improve actuator performance. The results are presented for three model variants:

- Variant I:
 - Coils with the same return;
 - Taking into account eddy currents.
- Variant II:
 - Reverse coils;
 - Taking into account eddy currents.
- Variant III:
 - Reverse coils;
 - Bypassing eddy currents.

Deriving results for the above three scenarios will allow a more in-depth assessment of the structure. Figure 19 shows the results for the hammer velocity during the working stroke. Figure 20 presents the axial component of the ponderomotive force acting on the ferromagnetic rings located in the hammer as well as the current in the coil as a function of the hammer's displacement.

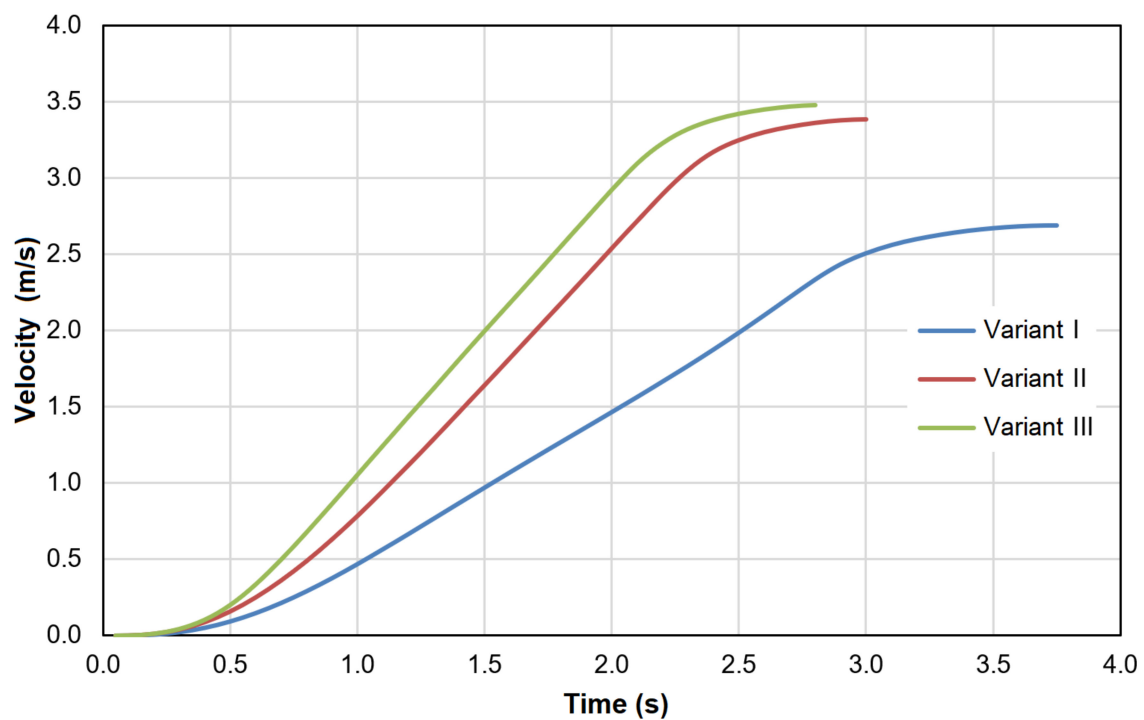


Figure 19. Hammer velocity vs. time for three variants of the calculation model.

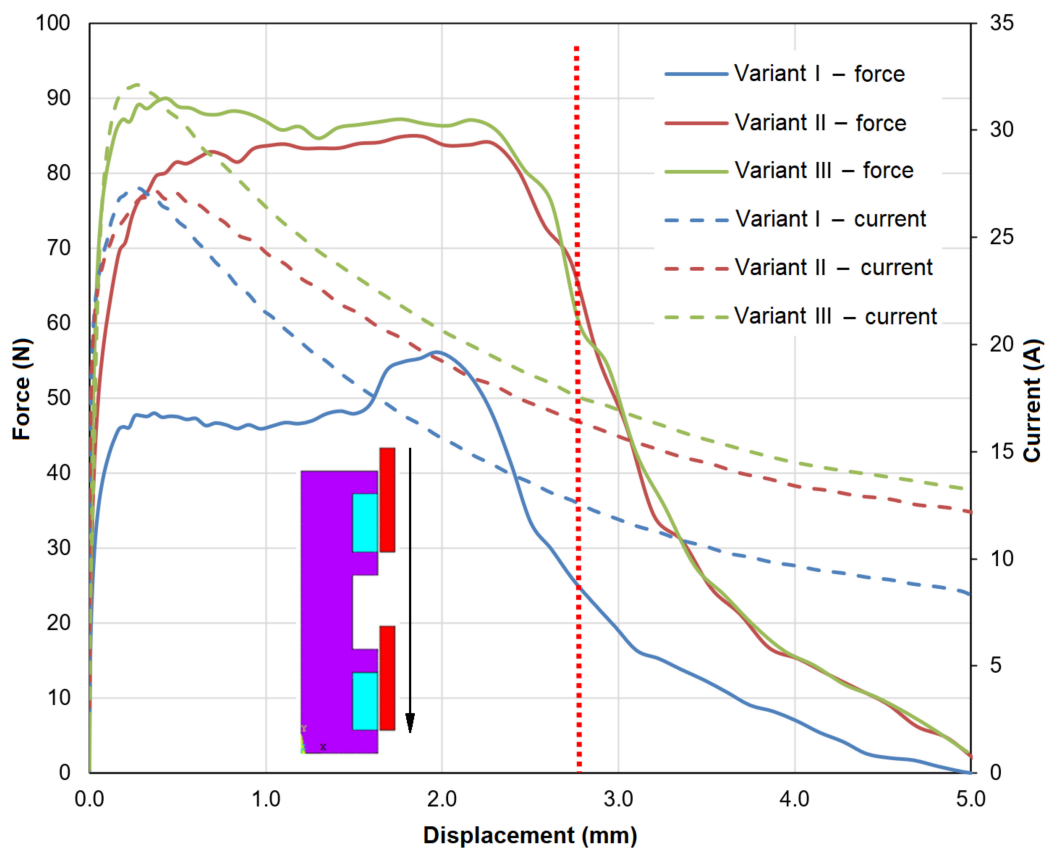
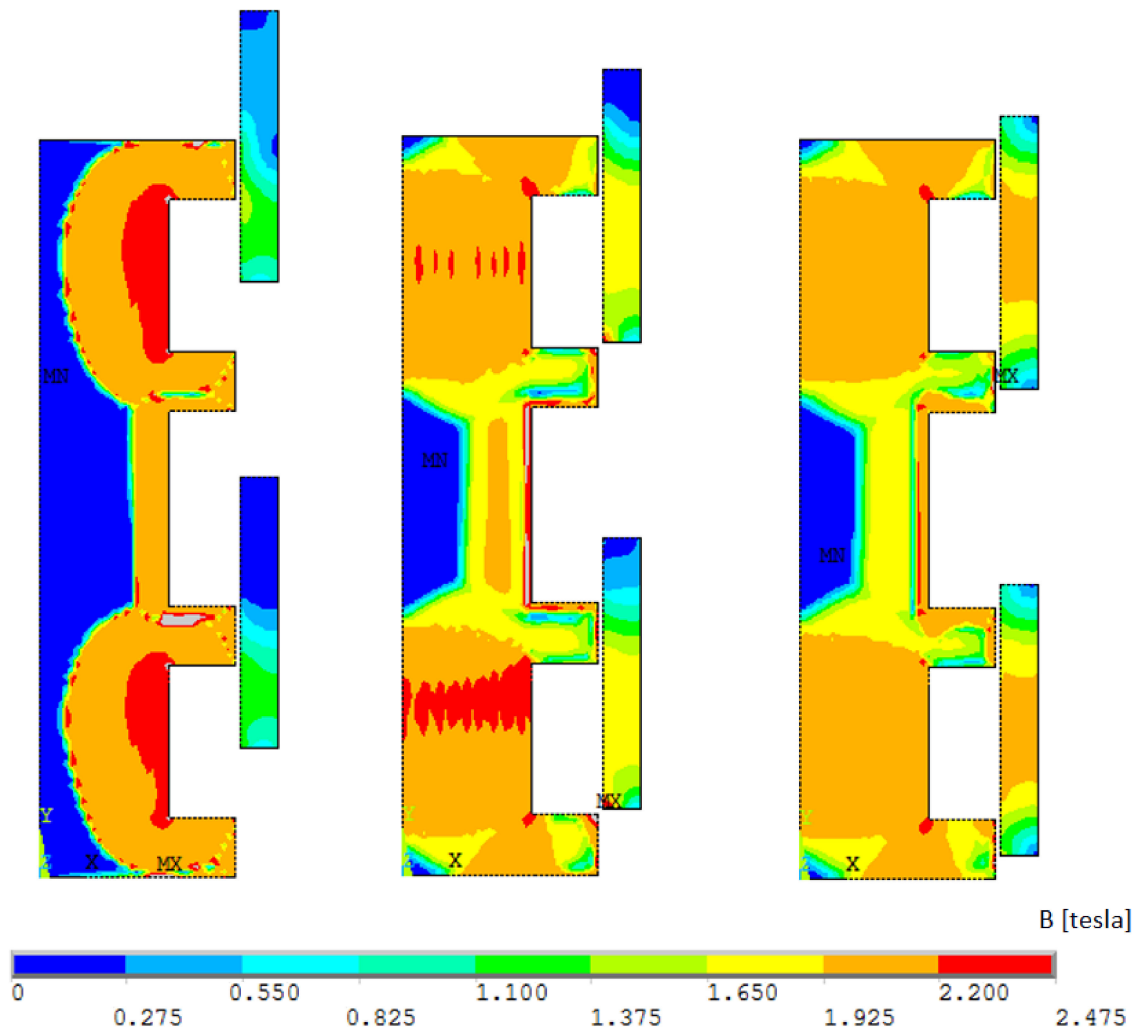


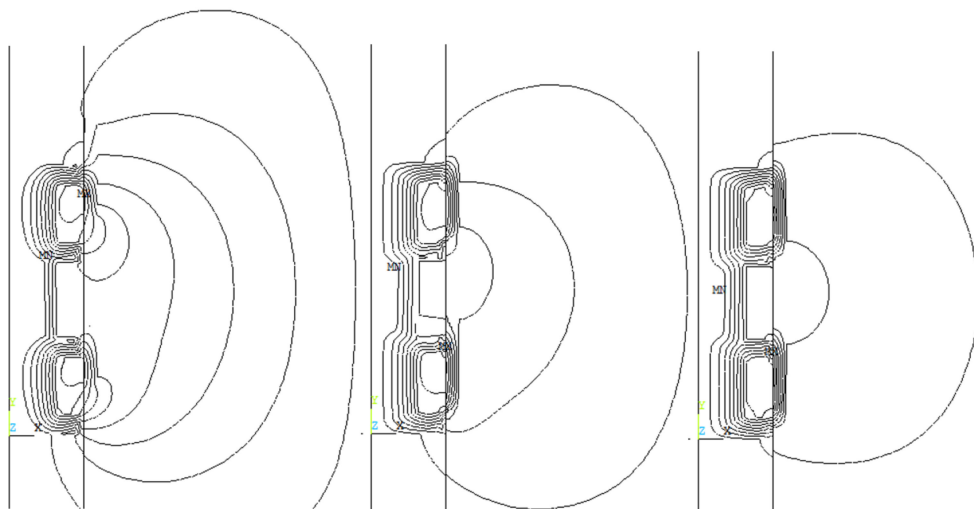
Figure 20. Ponderomotive force and current in the coil depending on the position of the hammer with the characteristic position of the ferromagnetic rings. Juxtaposition of results. Arrow marks the hammer displacement direction.

The FEM magnetic field simulation results are presented in Figures 21–23 below.

The simulation results in Figure 19 confirm the calculations beforehand and are in line with the theory of electromagnetism. It is obvious that for Variant I, even if the parasitic effects of eddy currents are taken into consideration, due to the incorrect winding of the coils, the velocity of the hammer is still at the lowest value. Maintaining the principle of push-wound coils for this case allows a significant increase in the final velocity. This is clearly shown in the course for Variant III. Unfortunately, in Variant III, there is the fault of the result related to the measurement of eddy current losses. The purpose of selecting such configured variants was to determine the percentage impact of model simplifications and thus the influence of eddy currents. The error of Variant II—which the authors indicate as the target, i.e., coils wound in opposite directions—considering the eddy currents is less than 10% in comparison to Variant III. The natural conclusion, referring to previous observations (Figure 19), is the simulation results from Figure 22. The results are related to the value of the ponderomotive force and current in the coil as a function of the position of the hammer with the position of the ferromagnetic rings. Despite the simplification, which is the presentation of the actuator core model as having a plane geometry with axial symmetry, the results of the tests and simulations carried out show very good compliance. This applies to both the value for the hammer velocity and the duration of the movement. Of course, this was possible due to the eddy current phenomenon as a boundary condition. Figures 21–23 show the magnetic induction field distribution for the three variants presented. Only for Variant II do the magnetic induction lines close through the core, hammer and air gap. It is worth noting that the correctness of the line closing is analogous for each hammer displacement (1 mm, 2.5 mm and 4 mm). A small part of the energy stored in the capacitors is dissipated. The value of this dispersion has a direct impact on the velocity of the hammer.

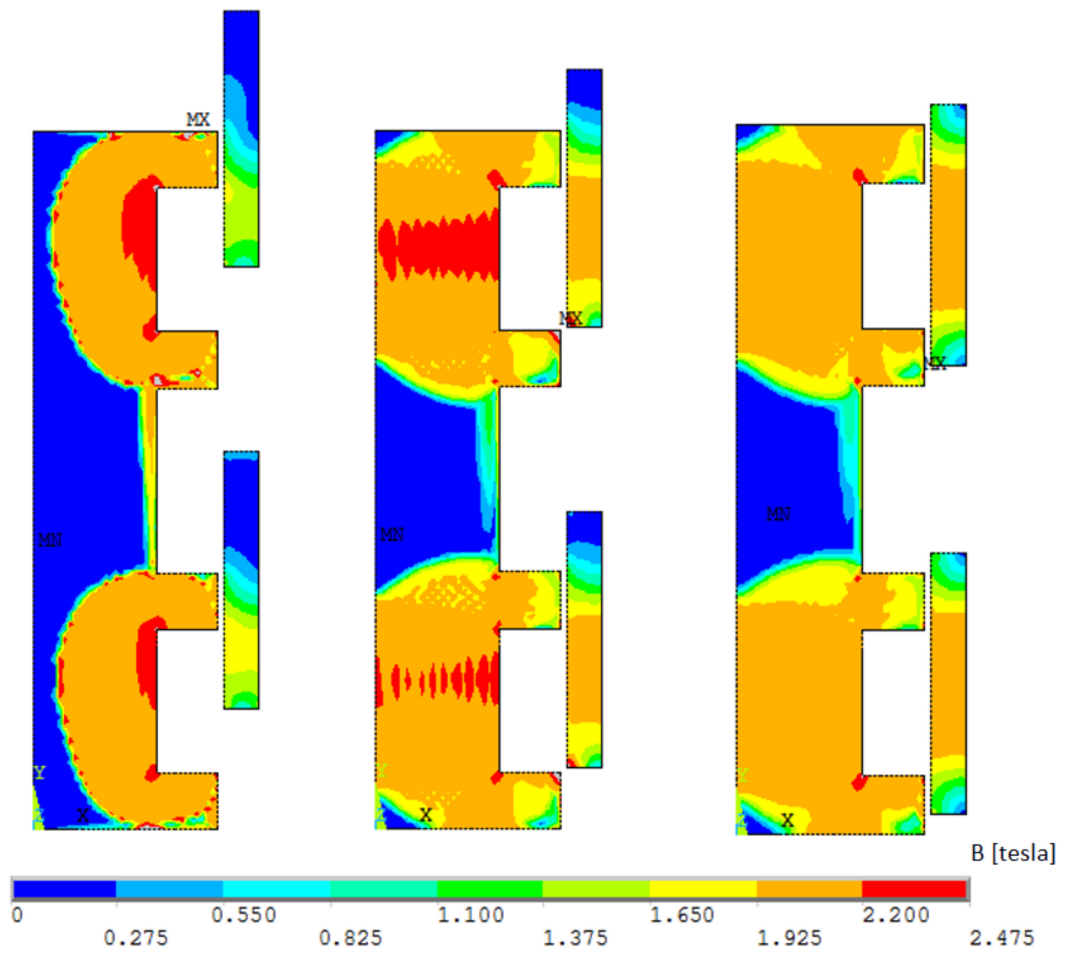


(a)

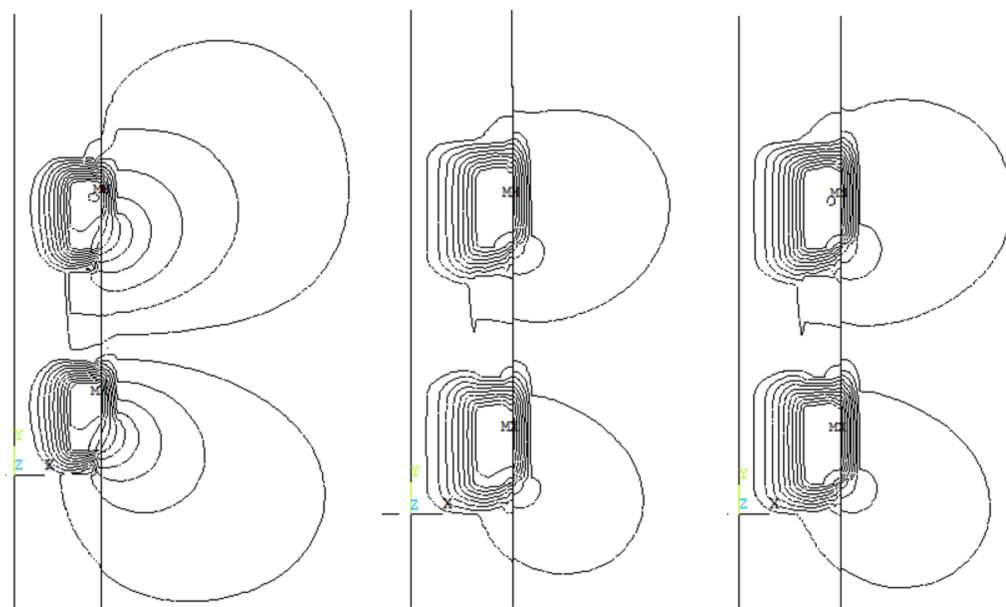


(b)

Figure 21. Magnetic field (a) and magnetic field lines (b) for hammer displacement (from the left): 1 mm, 2.5 mm and 4 mm—Variant I.



(a)



(b)

Figure 22. Magnetic field (a) and magnetic field lines (b) for hammer displacement (from the left): 1 mm, 2.5 mm and 4 mm—Variant II.

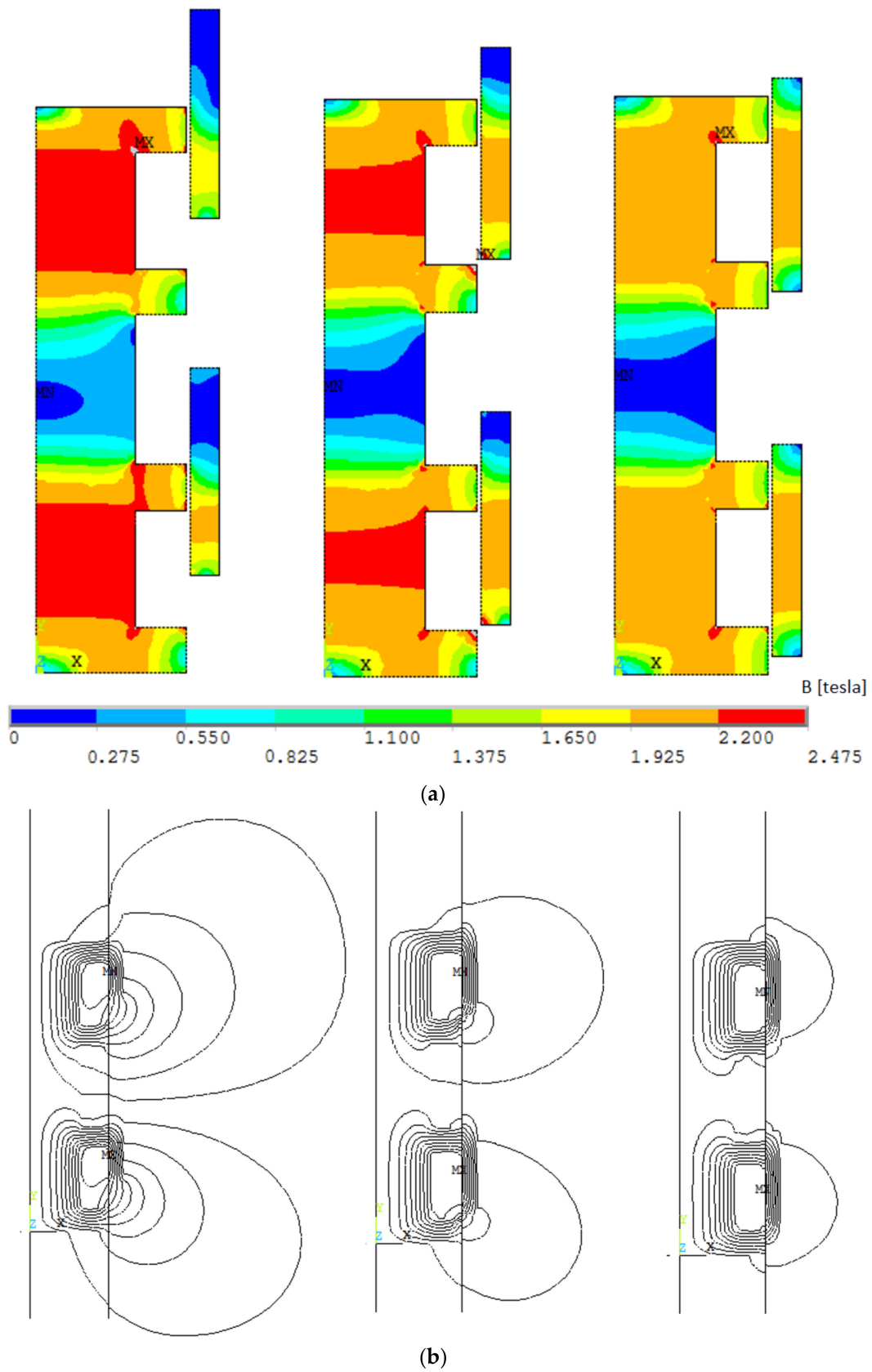


Figure 23. Magnetic field (a) and magnetic field lines (b) for hammer displacement (from the left): 1 mm, 2.5 mm and 4 mm—Variant III.

Figure 24 includes the simplified geometry of the device (without cuttings to reduce eddy current induction). It affects the eddy current FEM analysis. Even if such a phenomenon caused by the shape of the structure has not been taken into account, the boundary conditions should be properly selected. The magnetic induction values differ markedly in both cases. A result was obtained that confirmed previously acquired data (Figures 21 and 22).

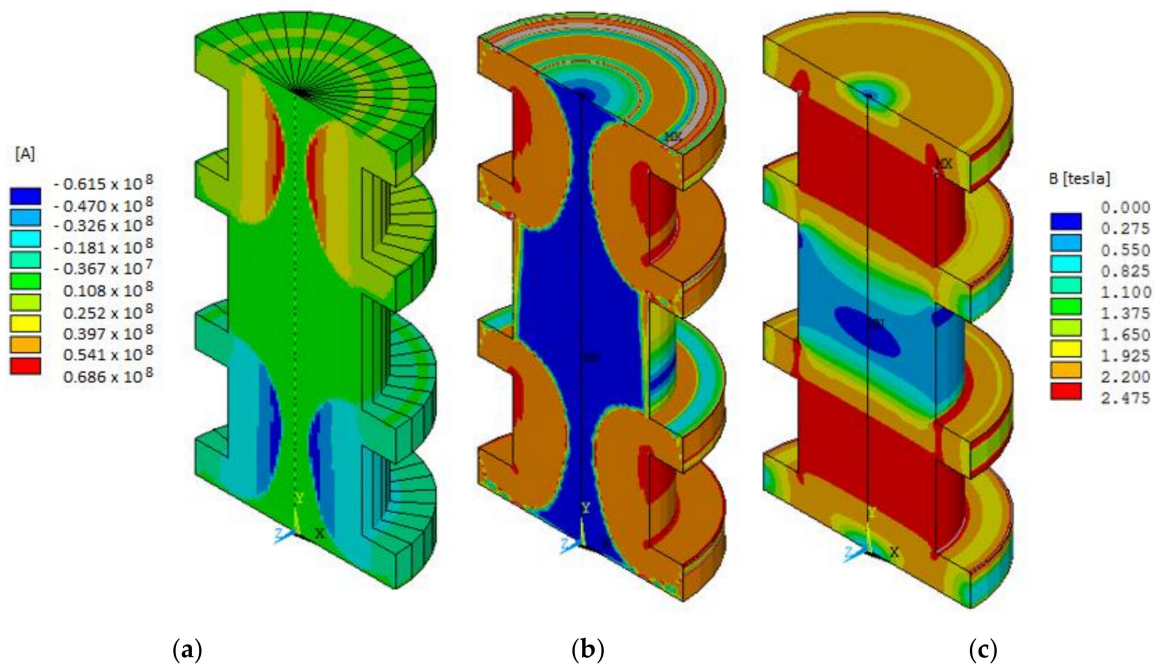


Figure 24. Eddy current analysis—(a) eddy current density; (b) value of magnetic induction in the core for analysis considering eddy currents; (c) value of magnetic induction in the core for analysis excluding eddy currents.

7. Conclusions

This manuscript presents a set of simulations for use in aerospace engineering involving important construction parameters such as eddy current impact, hammer displacement, and velocity. The overall electromagnetic analysis for different variants is also presented. Simulations may be treated as a method that allows the cost-effective design of such devices. The aerospace penetrator's construction principles were introduced, as was its overall functionality. A validated laboratory model and FEM simulations were presented for three different variants. The experimental and simulation results were juxtaposed and compared. Those were made in order to conclude the presented work. The effectiveness of the procedures was confirmed. The introduced procedure allows the shortening of the production time for the final product, as well as reducing costs. The model used was not limited in the representation of physical phenomena. For the multi-variant calculations of the tube reluctance actuator, the numerical model was described in Section 2. The purpose of the calculations was to determine the structural parameters ensuring the most efficient operation of the device. The specific use of the actuator implies the presentation of high-end values of these device parameters based on the derived results. Those are presented in Table 1 below. The best simulation results were acquired from Variant II, which consisted of the following boundary conditions: reversed coils and the inclusion of eddy currents. This scenario reflects the most frequent real conditions and provides valuable data for optimizing the functionality of the penetrator. It was noticed that not considering the eddy currents simplifies the model too much. Even if such a phenomenon caused by shape is not taken into account by the model construction, the boundary conditions must be selected accordingly. The induction values in both cases clearly differed. The results confirm the previous results received, as clearly shown in Figures 21 and 22.

Table 1. High-end parameters of the tube reluctance actuator derived after the laboratory model tests and simulation results.

Parameter	Value
Max. length of the actuator	127 (mm)
The outer diameter of the actuator (H)	22.7 (mm)
The total weight of the hammer	120 (g)
Total counter-mass weight	720 (g)
Energy stored in the capacitor	21 (J)

Author Contributions: Conceptualization, K.B., Ł.K. (Łukasz Kolimas), S.Ł., M.D., M.S., Ł.W., B.K., Ł.K. (Łukasz Kozarek); Data curation, K.B., Ł.K. (Łukasz Kolimas), S.Ł., M.D., M.S., Ł.W., B.K., Ł.K. (Łukasz Kozarek); Formal analysis, K.B., Ł.K. (Łukasz Kolimas), S.Ł., M.D., M.S., Ł.W., B.K., Ł.K. (Łukasz Kozarek); Investigation, K.B., Ł.K. (Łukasz Kolimas), S.Ł., M.D., M.S., Ł.W., B.K.; Methodology, K.B., M.D., Ł.W., B.K.; Project administration, K.B., Ł.K. (Łukasz Kolimas), S.Ł., M.D., M.S., Ł.W., B.K., Ł.K. (Łukasz Kozarek); Resources, K.B., M.D., Ł.W., B.K.; Supervision, K.B., M.D., Ł.W., B.K.; Validation, K.B., Ł.K. (Łukasz Kolimas), S.Ł., M.D., M.S., Ł.W., B.K.; Visualization, K.B., Ł.K. (Łukasz Kolimas), S.Ł., M.D., M.S., Ł.W., B.K.; Writing—original draft, K.B., Ł.K. (Łukasz Kolimas), S.Ł., M.D., M.S., Ł.W., B.K., Ł.K. (Łukasz Kozarek); Writing—review & editing, K.B., Ł.K. (Łukasz Kolimas), S.Ł., M.D., M.S., Ł.W., B.K., Ł.K. (Łukasz Kozarek). All authors have read and agreed to the published version of the manuscript.

Funding: This research received no external funding.

Conflicts of Interest: The authors declare no conflict of interest.

References

- Grygorczuk, J.; Banaszkiwicz, M.; Cichocki, A.; Ciesielska, M.; Dobrowolski, M.; Kędziora, B.; Krasowski, J.; Kuciński, T.; Marczewski, M.; Morawski, M.; et al. Advanced Penetrators and Hammering Sampling Devices for Planetary Body Exploration. In Proceedings of the ASTRA Conference ESA/ESTEC, Noordwijk, The Netherlands, 12 April 2011.
- Grygorczuk, J.; Banaszkiwicz, M.; Seweryn, K.; Spohn, T. MUPUS Insertion device for the Rosetta mission. *J. Telecommun. Inf. Technol.* **2007**, *1*, 50–53.
- Coste, P. Mobile penetrometer ground tests. In Proceedings of the 5th ESA Workshop on Advanced Space Technologies for Robotics and Automation—‘ASTRA 1998’, ESTEC, Noordwijk, The Netherlands, 1–3 December 1998.
- Richter, L.; Coste, P.; Gromov, V.V.; Kochan, H.; Nadalini, R.; Ng, T.C.; Pinna, S.; Richter, H.E.; Yung, K.L. Development and testing of subsurface sampling devices for the Beagle-2 lander. *Planet. Space Sci.* **2002**, *50*, 903–913. [[CrossRef](#)]
- Knollenberg, J.; Nadalini, R.; Spohn, T. Thermal measurements with HP3/TEM on ExoMars. *Geophys. Res. Abstr.* **2007**, *9*, 441–447.
- Mirzaee, M.; Hooshmand, P.; Ahmadi, H.; Balotaki, H.K.; KhakRah, H.; Jamalabadi, M.Y.A. Electromagnetohydrodynamic Effects on Steam Bubble Formation in Vertical Heated Upward Flow. *Energies* **2016**, *9*, 657. [[CrossRef](#)]
- Ma, F.; Yin, H.; Wei, L.; Wu, L.; Gu, C. Analytical Calculation of Armature Reaction Field of the Interior Permanent Magnet Motor. *Energies* **2018**, *11*, 2375. [[CrossRef](#)]
- Kolimas, Ł.; Łapczyński, S.; Szulborski, M.; Świetlik, M. Low Voltage Modular Circuit Breakers: FEM Employment for Modelling of Arc Chambers. *Bull. Pol. Acad. Sci. Tech. Sci.* **2020**, *68*, 1–10.
- Nadalini, R.; Spohn, T.; Ambrosi, R.; Ball, A.J.; Frasier, G.; Grzesik, A.; Hagermann, A.; Hall, C.; Knollenberg, J.; Lichopoj, A.; et al. The Heat flow and Physical Properties Package (HP3) an integrated sensor suite for planetary subsurface investigations. *Geophys. Res. Abstr.* **2006**, *8*, 5.
- Banerdt, B.; Smrekar, S.; Dehant, V.; Lognonné, P.; Spohn, T.; Grott, M. GEMS (GEophysical Monitoring Station). In Proceedings of the EPSC-DPS Joint Meeting, Nantes, France, 7 October 2011.

11. Stoker, C.R.; Richter, L.; Smith, W.H.; Lemke, L.G.; Hammer, P.; Dalton, J.B.; Glass, B.; Zent, A. The Mars Underground Mole (MUM): A Subsurface Penetration Device with In Situ Infrared Reflectance and Raman Spectroscopic Sensing Capability. In Proceedings of the 34th Annual Lunar and Planetary Science Conference, League City, TX, USA, 12 March 2003.
12. Kolimas, L.; Łapczyński, S.; Szulborski, M. Tulip contacts: Experimental studies of electrical contacts in dynamic layout with the use of FEM software. *Int. J. Electr. Eng. Educ.* **2019**, *1*, 1–4. [[CrossRef](#)]
13. Gromov, V.V.; Mischevich, A.V.; Yudkin, E.N.; Kochan, H.; Coste, P.; Re, E. The mobile penetrometer, a “mole” for sub-surface soil investigation. In Proceedings of the 7th European Space Mechanisms & Tribology Symposium, ESTEC, Noordwijk, The Netherlands, 10 October 1997.
14. Grygorczuk, J.; Banaszkiwicz, M.; Kargl, G.; Kömle, N.; Ball, A.J.; Seweryn, K. Use of hammering to determine cometary nucleus mechanical properties. Penetrometry in the Solar System II. In Proceedings of the 2nd International Workshop on Penetrometry in the Solar System, Graz, Austria, 1–4 September 2009; Austrian Academy of Sciences Press: Berlin, Germany, 2009; pp. 93–107.
15. Grygorczuk, J. Key Problems of Design, Modeling and Application of Cometary Auto Penetrator MUPUS (In Polish: Kluczowe Problem Projektowania, Modelowania i Aplikacji Autopenetratora Kometarnego MUPUS). Ph.D. Thesis, Faculty of Power and Aeronautical Engineering, Warsaw University of Technology, Warsaw, Poland, 2010.
16. Grygorczuk, J.; Seweryn, K.; Wawrzaszek, R.; Banaszkiwicz, M. Technological features in the new mole penetrator ‘KRET’. In Proceedings of the 13th European Space Mechanisms and Tribology Symposium (ESMATS), Vienna, Austria, 23 September 2009.
17. Grygorczuk, J.; Kędziora, B.; Tokarz, M.; Seweryn, K.; Banaszkiwicz, M.; Dobrowolski, M.; Łyszczek, P.; Rybus, T.; Sidz, M.; Skup, K.; et al. *Ultra-Light Planetary Manipulator-Study and Development. Submitted to: Geoplanet: Earth and Planetary Science*; Springer: Berlin/Heidelberg, Germany, 2012.
18. Grygorczuk, J.; Dobrowolski, M.; Wisniewski, L.; Banaszkiwicz, M.; Ciesielska, M.; Kędziora, B.; Seweryn, K.; Wawrzaszek, R.; Wierzchon, T.; Trzaska, M.; et al. Advanced mechanisms and tribological tests of the hammering sampling device CHOMIK. In Proceedings of the 14th European Space Mechanisms and Tribology Symposium (ESMATS), Constance, Germany, 28 September 2011.
19. Glassmeier, K.H.; Boehnhardt, H.; Koschny, D.; Kührt, E.; Richter, I. The Rosetta Mission: Flying Towards the Origin of the Solar System. *Space Sci. Rev.* **2007**, *128*, 1–21. [[CrossRef](#)]
20. Banaszkiwicz, M.; Seweryn, K.; Wawrzaszek, R. Thermal conductivity determination of cometary and asteroid materials. *Adv. Space Res.* **2007**, *40*, 226–237. [[CrossRef](#)]
21. Spohn, T.; Seiferlin, K.; Hagermann, A.; Knollenberg, J.; Ball, A.J.; Banaszkiwicz, M.; Benkhoff, J.; Gadomski, S.; Grygorczuk, J.; Hlond, M.; et al. MUPUS—A Thermal and Mechanical Properties Probe for the Rosetta Lander PHILAE. *Space Sci. Rev.* **2007**, *128*, 339–362. [[CrossRef](#)]
22. Grygorczuk, J.; Seweryn, K.; Banaszkiwicz, M.; Ciesielska, M.; Dobrowolski, M.; Kędziora, B.; Rybus, T.; Sidz, M.; Tokarz, M.; Wawrzaszek, R. MUPUS, CHOMIK AND KRET Penetrators as Examples of Mechanisms Used as End-Effectors of Manipulators in Space Exploration Missions. *Pr. Nauk. Elektron. Pos. Robot.* **2012**, *z.182*, 503–512. (In Polish)
23. Seweryn, K.; Banaszkiwicz, M.; Bednarz, S.; Gonet, A.; Grygorczuk, J.; Rybus, T.; Rzycki, M.; Wawrzaszek, R.; Wisniewski, L.; Wojcikowski, M. Mole Penetrator ‘KRET’ for 446 Lunar Exploration. In Proceedings of the 42th Lunar and Planetary Science Conference, The Woodlands, TX, USA, 7–11 March 2011.
24. Gurgurewicz, J.; Rickman, H.; Królikowska, M.; Banaszkiwicz, M.; Grygorczuk, J.; Morawski, M.; Seweryn, K.; Wawrzaszek, R. Phobos investigations using the CHOMIK device (Phobos Sample Return mission). In Proceedings of the First Moscow Solar System Symposium, Moscow, Russia, 11–15 October 2010.
25. Grygorczuk, J.; Seweryn, K.; Rickman, H.; Morawski, M.; Aleksashkin, S.N.; Banaszkiwicz, M.; Ciesielska, M.; Dobrowolski, M.; Drogosz, M.; Gurgurewicz, J.; et al. CHOMIK sampling device for Russian Phobos Sample Return Mission. In Proceedings of the First Moscow Solar System Symposium, Moscow, Russia, 11–15 October 2010.
26. Seweryn, K.; Aleksashkin, S.N.; Banaszkiwicz, M.; Cichocki, A.; Ciesielska, M.; Dobrowolski, M.; Gurgurewicz, J.; Grygorczuk, J.; Kędziora, B.; Krasowski, J.; et al. The CHOMIK Instrument for Phobos-Grunt Mission-Functional Test and Calibration Data. In Proceedings of the 2nd Moscow Solar System Symposium, Moscow, Russia, 26 August 2011.

27. Dabrowski, B.; Banaszekiewicz, M. Measurement of lunar and Martian regolith thermal properties using subsurface robotic teams. In Proceedings of the 9th ESA Workshop on Advanced Space Technologies for Robotics and Automation, Noordwijk, The Netherlands, 28–30 November 2006.
28. Surkov, Y.A.; Kremnev, R.S. Mars-96 mission: Mars exploration with the use of penetrators. *Planet. Space Sci.* **1998**, *46*, 1689–1696. [[CrossRef](#)]
29. Lorenz, R.D.; Moersch, J.E.; Stone, J.A.; Morgan, A.R., Jr.; Smrekar, S.E. Penetration tests on the DS-2 Mars microprobes: Penetration depth and impact accelerometry. *Planet. Space Sci.* **2000**, *48*, 419–436. [[CrossRef](#)]
30. Nakajima, T.; Hinada, M.; Saitoh, H.; Kawaguchi, J.I.; Akio, F. Lunar penetrator program: Lunar-A. *Acta Astronaut.* **1996**, *39*, 111–119. [[CrossRef](#)]
31. Lichtenheldt, R. Hammering beneath the surface of Mars-modeling and simulation of the impact-driven locomotion of the HP3-Mole by coupling enhanced multi-body dynamics and discrete element method. In Proceedings of the 58th Ilmenau Scientific Colloquium, Ilmenau, Germany, 8–12 September 2014; pp. 155–174.
32. Nagaoka, K.; Kubota, T.; Otsuki, M.; Tanaka, S. Experimental study on autonomous burrowing screw robot for subsurface exploration on the Moon. *Intell. Robot. Syst.* **2008**, *4*, 4104–4109.
33. Lu, Z.S.; Cao, D.H. Simulation analysis for physical model of stick-slip. *Chin. J. Mech. Eng.* **2004**, *40*, 107–112. [[CrossRef](#)]
34. Liu, L.L.; Liu, H.Z.; Wu, Z.Y.; Wang, Z.M. An overview of friction models in mechanical systems. *Adv. Mech.* **2008**, *38*, 201–213.
35. Grygorczuk, J.; Banaszekiewicz, M.; Seweryn, K.; Wiśniewski, Ł.; Wawrzaszek, R. Space Penetrators- Rosetta case study. In Proceedings of the 18th International Conference on Methods & Models in Automation & Robotics (MMAR), Międzyzdroje, Poland, 26–29 August 2013.
36. Shen, Y.; Jiang, S.; Xu, C.; Zhang, W.; Wu, X. Study on Optimization of Structure Parameters to the Penetrator. In Proceedings of the IEEE International Conference on Mechatronics and Automation, Harbin, China, 7–10 August 2016.
37. Barmpatza, A.C.; Kappatou, J.C. Finite Element Method Investigation and Loss Estimation of a Permanent Magnet Synchronous Generator Feeding a Non-Linear Load. *Energies* **2018**, *11*, 3404. [[CrossRef](#)]
38. Grygorczuk, J.; Wiśniewski, Ł.; Banaszekiewicz, M.; Ciesielska, M.; Dobrowolski, M.; Kedziora, B.; Krasowski, J.; Przybyła, R.; Seweryn, K.; Tokarz, M.; et al. High energy and efficiency penetrator-heap. In Proceedings of the 15th European Space Mechanisms & Tribology Symposium-ESMATS 2013, Noordwijk, The Netherlands, 25–27 September 2013.



© 2020 by the authors. Licensee MDPI, Basel, Switzerland. This article is an open access article distributed under the terms and conditions of the Creative Commons Attribution (CC BY) license (<http://creativecommons.org/licenses/by/4.0/>).